

Synchrotron Radiation Spectroscopic Studies of Mg²⁺ Storage Mechanisms in High-Performance Rechargeable Magnesium Batteries with Co-Doped FeS₂ Cathodes

Hao Xu, Yue Li, Dong Zhu, Zhao Li, Fengzhan Sun, Wen Zhu, Yu Chen, Jichao Zhang, Li Ren, Saihang Zhang, Jianxin Zou,* and Richard M. Laine*

Rechargeable magnesium batteries (RMBs) are one of the more promising future energy storage systems. This work proposes a non-nucleophilic phenolate-based magnesium complex (PMC) electrolyte enabling reversible Mg stripping/plating with a low over-potential of 84.3 mV at 1 mA cm⁻². Subsequently, Co doping is introduced to prepare FeS₂, Fe_{0.9}Co_{0.1}S₂, Fe_{0.75}Co_{0.25}S₂ and Fe_{0.5}Co_{0.5}S₂. Multiple characterizations confirm that Co doping can expand the crystal lattice and reduce particle sizes, thus benefiting cathode reactions. With Co doping, Fe orbitals can be expected to transform from high spin to low spin states without valence changes while the spin state of Co atoms is little influenced. Then, Co-doped FeS₂ cathodes coated on copper collectors coupling with a PMC electrolyte for RMBs show superior electrochemical performance among reported chalcogenide cathodes, displaying a maximum discharge capacity (700 mAh g⁻¹) at 0.1 A g⁻¹. Specifically, Fe_{0.5}Co_{0.5}S₂ cathodes exhibit the best cycling stability and shortest activation time. Even at 1 A g⁻¹, a discharge capacity (164 mAh g⁻¹) is still achieved after 1000 cycles. Mechanistic studies indicate that copper collector participates in the cathode reactions accompanied by Cu_{1.8}S generation while Fe and Co species play a synergistic catalytic role, providing effective tactics for rational design of electrolytes, conversion type cathodes, and collectors.

raising considerable potential utility. Magnesium is the eighth most abundant element in the earth's crust, accounting for about 2 wt%.^[2] Mature magnesium smelting technology and wide application of Mg-based materials in energy storage,^[3] medical and other fields make the price of Mg much lower than that of Li.^[4] Previous work has proven that Mg anodes do not suffer significantly from dendrite formation during RMB cycling due to its low chemical reactivity,^[5] also providing a high theoretical volumetric capacity (3832 mAh cm⁻³).^[6] However, a magnesium oxide layer forms easily on Mg anode surfaces impeding Mg²⁺ diffusion.^[7] Given the immense potential offered by RMBs, it is imperative that a resolution to current problems concerning the compatibility between Mg anodes, electrolytes, and appropriate cathode materials should be explored.

Cathode materials can be both intercalation and conversion types. The strong coulombic interactions between Mg²⁺ and intercalation matrices lead to sluggish solid-state diffusion, rendering cathode materials poor ion conductors.^[8] The regulation of the Mg²⁺-solvation structure in electrolyte and crystal lattice spacing for materials offers two effective avenues to improve

1. Introduction

Rechargeable magnesium batteries (RMBs) provide great potential for the safe and large-scale energy storage with low cost,^[1]

H. Xu, Z. Li, F. Sun, W. Zhu, L. Ren, S. Zhang, J. Zou
National Engineering Research Center of Light Alloy Net Forming School
of Materials Science and Engineering & State Key Laboratory of Metal
Matrix Composites
School of Materials Science and Engineering
Shanghai Jiao Tong University
Shanghai 200240, P. R. China
E-mail: zoujx@sjtu.edu.cn


H. Xu, Z. Li, F. Sun, W. Zhu, L. Ren, S. Zhang, J. Zou
Center of Hydrogen Science
Shanghai Jiao Tong University
Shanghai 200240, P. R. China

Y. Li
Shanghai Key Laboratory of Magnetic Resonance
School of Physics and Electronic Science
East China Normal University
Shanghai 200241, P. R. China

D. Zhu
University of Chinese Academy of Science
Beijing 100049, P. R. China

Y. Chen, J. Zhang
Shanghai Synchrotron Radiation Facility
Shanghai Advanced Research Institute
Chinese Academy of Sciences
Shanghai 201204, P. R. China

R. M. Laine
Department of Materials Science and Engineering
University of Michigan
Ann Arbor, MI 48109-2136, USA
E-mail: talsdad@umich.edu

 The ORCID identification number(s) for the author(s) of this article can be found under <https://doi.org/10.1002/aenm.202201608>.

DOI: 10.1002/aenm.202201608

reaction kinetics and cycling stability.^[9] However, this will likely increase costs and time for electrolyte and material syntheses. Conversion type cathodes can be free from the kinetic inhibition of Mg^{2+} insertion/extraction,^[10] always exhibiting high specific capacity and long-term cycling performance. Such “ideal” conversion materials are non-metallic simple substances belonging to group VIA including O₂, S, Se, and Te with high theoretical volumetric capacities and widespread natural abundance.^[11]

Magnesium sulfur batteries (MSBs) using S cathodes have been studied widely since HMDSMgCl/AlCl₃ electrolyte was identified as being viable for the MSB prototype.^[12] Later, a myriad of electrolytes were prepared and reported to improve MSB performance,^[6a,13] focusing on non-nucleophilic properties and the compatibility between Mg anodes, S cathodes, and electrolytes. These electrolytes are always prepared using Mg(HMDS)₂,^[14] Mg(CB₁₁H₁₂)₂,^[15] Mg(TFSI)₂,^[16] Mg(CF₃SO₃)₂,^[17] Mg[B(hfip)₄]₂ salts,^[18] rendering synthesis costs quite high, which is far from practical application. In addition, MSBs still suffer from the shuttling of magnesium polysulfides, low actual specific capacity, and short cycle life.^[19]

Metal sulfides (MS_x) with lower theoretical specific capacities than sulfur could be suitable conversion type materials,^[6b,20] where metal can enhance reaction kinetics during RMB cycling. In a manner, MS_x can serve as another form of sulfur. The “M” can be hypothetically regarded as zero valence and S in MS_x could also be also zero valence. As for conversion type cathodes of RMBs, metal (M) can be divided into two types. Type I is a Mg alloy including M like Sn, Sb, and Bi.^[21] In type II systems, Mg does not react with M, e.g., 3d transition metals.^[9c,22] Even though S has a high theoretical specific capacity of 1675 mAh g⁻¹, Table S1 (Supporting Information) shows that M in MS_x materials reduces generally specific capacities compared with pure sulfur. In theory, VS₄ (S content = 71.6 wt%) has a high theoretical specific capacity based on the assumed conversion of V⁰-S₄⁰ to V⁰-4MgS. Nevertheless, VS₄ is reported to be an intercalation type material and the conversion of VS₄ to V-MgS occurs rarely,^[23] making the actual specific capacity relatively low. In contrast, alloying-type metal sulfides like Sb₂S₃, SnS₂ and Bi₂S₃ could be good choices for RMBs. However, insufficient researches have been devoted to their study and to date they tend to demonstrate unsatisfactory electrochemical performance.^[24]

The type II metal sulfides have been widely studied. When CuS cathodes with different modified morphologies are used for RMBs,^[25] they show a maximum capacity of 477 mAh g⁻¹ at 0.05 A g⁻¹ though cycling life is only 60 cycles. Pyrite FeS₂ with considerable sulfur content (53.4 wt%) offers the advantages of an abundant resource and a simple synthesis providing potential toward high energy densities. FeS₂ has a high theoretical capacity of 896 mAh g⁻¹ and the corresponding mass energy density is 1200 Wh kg⁻¹. Unfortunately, previous work by Mao et al. finds that FeS₂ cathodes show extremely poor electrochemical performance and capacities are contributed by Mg²⁺ insertion/extraction.^[22c]

Also, the strategies of using additives like Li⁺ and Na⁺ salts were proposed to enhance the electrochemical performance.^[26] Another study reported that FeS₂ cathodes delivered a capacity of 600 mAh g⁻¹ after 50 cycles at 0.05 A g⁻¹ when coupled with a copper current collector.^[27] Even though copper was proven to participate in the cathode reactions during first cycle, the reac-

tion mechanism was not clear as the cell reaches its maximum capacity, implying an activation process. Besides, expensive non-nucleophilic Mg(HMDS)₂, Mg(TFSI)₂, Mg[B(hfip)₄]₂ based salts are always used for these RMBs, making the road from laboratory research to application particularly long. Therefore, considerable impetus remains to develop an efficient, in-expensive and non-nucleophilic electrolyte for RMBs using conversion-type cathodes.

In this study, inspired by the efficient solution structure of widely used all phenyl complex [(PhMgCl)₂-AlCl₃/THF, APC] electrolyte,^[8a,28] nucleophilic Ph⁻ groups were replaced with R-Ph-O⁻ groups to prepare the (R-PhOMgCl)₂-AlCl₃/THF electrolyte where R is the alkyl group of 2-tert-butyl-4-methylphenol, namely phenolate-based magnesium complex (PMC) electrolyte.^[29] Here, O⁻ is less nucleophilic compared with C⁻. Simultaneously, the 2p orbital electrons of O⁻ will conjugate with π electrons of benzene ring, thus lowering the nucleophilicity, for use as described below. Table S2 (Supporting Information) shows that the synthesis cost of this electrolyte is much less than other typical electrolytes. Additionally, we adopt the strategy of using dopants as they are known to improve the performance of materials used in electrocatalysis, photocatalysis, and energy storage.^[30] First, Co-doped FeS₂ cathodes with Co doping ratios of 0, 10, 25, and 50 at% (denoted as FeS₂, Fe_{0.9}Co_{0.1}S₂, Fe_{0.75}Co_{0.25}S₂ and Fe_{0.5}Co_{0.5}S₂, respectively) were prepared via simple hydrothermal syntheses and characterized in detail (see below). Characterization results show that Co replaces Fe in the same crystallographic positions.

RMBs using Co-doped FeS₂ cathodes, PMC electrolyte, and copper collectors show good electrochemical performance compared with other conversion type cathodes (Table S3, Supporting Information). FeS₂ cathodes now offer a highest discharge capacity of 700 mAh g⁻¹ at 0.1 A g⁻¹. Fe_{0.5}Co_{0.5}S₂ cathodes have the shortest activation of 14 cycles and maintain a discharge capacity of 613 mAh g⁻¹ after 150 cycles at 0.1 A g⁻¹, even displaying a high discharge capacity of 164 mAh g⁻¹ after 1000 cycles at 1 A g⁻¹. Last but not least, the reaction of Mg²⁺ with Co-doped FeS₂ plays a dominant role in contributing to capacity during initial RMB cycling. Reactions at the copper collector with Co-doped FeS₂ are part of the activation process, accompanied by generation of Cu_{1.8}S. Deservedly, Mg²⁺ reactions with Cu_{1.8}S play a leading role after sufficient cycling while the Fe and Co species can act as catalysts to improve the reaction kinetics, clarifying the roles of Fe, Co, and Cu. Briefly, this work inspired us to consider the actions of copper collector in electrodes for other batteries like rechargeable lithium/sodium/zinc/aluminum ion batteries. Moreover, it should make PMC electrolyte attractive for RMBs, which can be better regulated for further studies.

2. Results and Discussion

2.1. The Structure of Co-Doped FeS₂ Materials

A simple hydrothermal method was used to prepare Co-doped FeS₂ materials. **Figure 1a** provides a general overview of the processing steps (see experimental section, Supporting Information). The prepared FeS₂, Fe_{0.9}Co_{0.1}S₂, Fe_{0.75}Co_{0.25}S₂ and Fe_{0.5}Co_{0.5}S₂ samples were characterized by X-ray diffraction

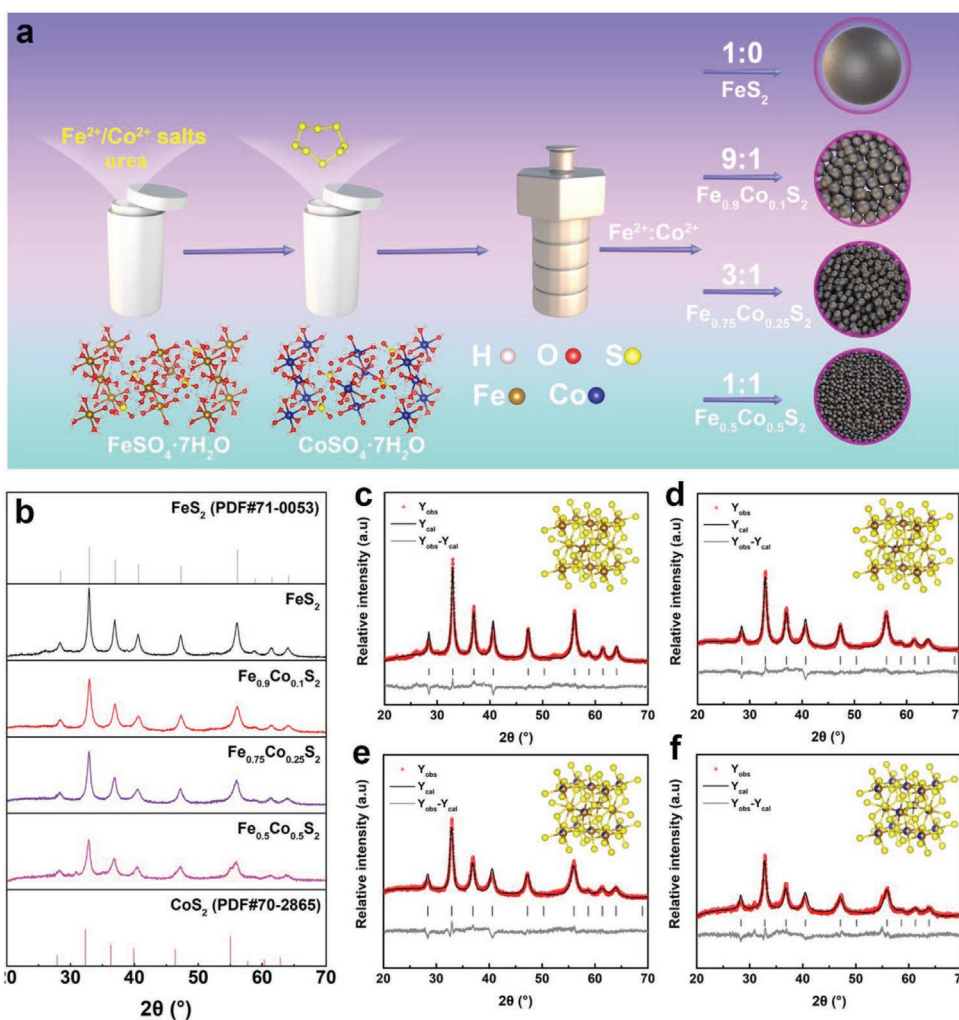


Figure 1. a) General methods used to prepare $\text{Fe}_{1-x}\text{Co}_x\text{S}_2$ ($x = 0, 0.1, 0.25, 0.5$) samples. b) XRD patterns of these samples. Rietveld refinement results of the as-prepared c) FeS_2 , d) $\text{Fe}_{0.9}\text{Co}_{0.1}\text{S}_2$, e) $\text{Fe}_{0.75}\text{Co}_{0.25}\text{S}_2$ and f) $\text{Fe}_{0.5}\text{Co}_{0.5}\text{S}_2$.

(XRD). Figure 1b shows that characteristic diffraction patterns of as-obtained samples can be indexed to standard pyrite FeS_2 (JCPDs. card 71-0053), with a space group of $Fm-3m$, confirming successful Co doping. Moreover, all diffraction peaks shift slightly to a lower angle compared with those of pyrite CoS_2 (JCPDs. card 70-2865). With increasing the Co content, the diffraction peaks become weaker and broader, indicating the decreased crystallinity and reduced particle sizes. The XRD pattern of $\text{Fe}_{0.5}\text{Co}_{0.5}\text{S}_2$ displays a weak peak at 30.9° , likely attributable to traces of impurities. At an anticipated doping content of 75%, the XRD pattern of “ $\text{Fe}_{0.25}\text{Co}_{0.75}\text{S}_2$ ” (Figure S1, Supporting Information) does not match with pyrite FeS_2 or CoS_2 , indicating the unsuccessful preparation. Thus, 50 at% is the highest content of Co dopant in this study.

To further understand the results mentioned above, Rietveld refinement of XRD patterns was performed using the Pseudo-Voigt profile fitting function.^[31] The results are shown in Figure 1c–f and detailed data are provided in Table S4 (Supporting Information). Note that 10 at% doping causes the formation of a slight smaller unit cell. With increasing Co doping ratios, the unit-cell gradually expands as M–S

(M = Fe/Co) bonds lengthen. For typical conversion-type metal sulfides, metal–sulfur bonds should transform to Mg–S bonds during RMB discharge. Specifically, M–S (M = Fe/Co) bonds lengthen as M–S bond strength lessens. This is advantageous as cleavage of M–S bonds to produce Mg–S bonds becomes energetically more favorable. Doping Co in FeS_2 could be an effective strategy to realize reversible reactions during battery cycling as suggested by $\text{M–S} + \text{Mg} \leftrightarrow \text{Mg–S} + \text{M}$.

Materials’ morphology and compositional evolution were first characterized by scanning electron microscopy (SEM). As shown in Figure S2a (Supporting Information), FeS_2 without Co exhibits a spherical morphology with a rough surface and diameters of several microns. Figure S2f,k,p (Supporting Information) show that Co doping reduces average particle sizes (APSS) and causes agglomeration. Energy dispersive X-ray (EDX) microscopy analyses (Figure S2 and Table S5, Supporting Information) reveal a Fe:S molar ratio of 0.33:0.67 for FeS_2 . Similar findings are found for homogeneous distributions of Fe, Co, S for $\text{Fe}_{1-x}\text{Co}_x\text{S}_2$ ($x = 0.1, 0.25, 0.5$) samples with Fe:Co:S molar ratios close to the feeding ratio. Nevertheless, Figure S3a–e (Supporting Information) shows that the

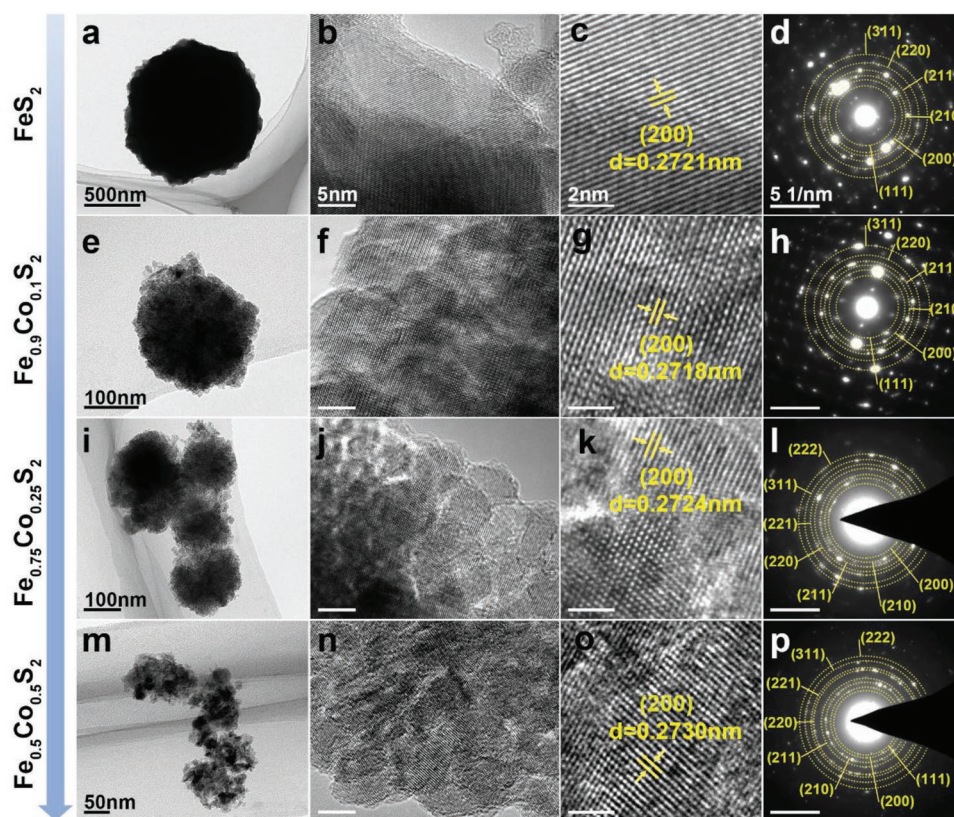


Figure 2. TEM images, HRTEM images at different magnifications, SAED patterns of as-prepared a–d) FeS_2 , e–h) $\text{Fe}_{0.9}\text{Co}_{0.1}\text{S}_2$, i–l) $\text{Fe}_{0.75}\text{Co}_{0.25}\text{S}_2$ and m–p) $\text{Fe}_{0.5}\text{Co}_{0.5}\text{S}_2$ samples. (The scale bars of Figure b, f, j, n are 5 nm; the scale bars of Figure c, g, k, o are 2 nm and the scale bars of Figure d, h, l, p are 5 \AA).

Fe:Co:S molar ratio of as-prepared $\text{Fe}_{0.75}\text{Co}_{0.25}\text{S}_2$ sample deviates greatly, verifying the unsuccessful preparation of objective “ $\text{Fe}_{0.25}\text{Co}_{0.75}\text{S}_2$ ”, agreeing well with the XRD analyses. Additionally, the Fe:Co:S molar ratio of as-anticipated “ $\text{Fe}_{0.1}\text{Co}_{0.9}\text{S}_2$ ” presented in Figure S3f–j (Supporting Information) deviates greatly from the feeding ratio, further confirming that excessive Co doping inhibits pyrite phase formation.

Transmission electron microscopy (TEM) allows clearer assessment of sample morphologies and structures. As Co doping increases from 0 to 50 at%, low-resolution TEM images in Figure 2a,e,i,m reveal decreases in APSs, consistent with the SEM observations. Co^{2+} in solution seems to inhibit particle growth during hydrothermal processing. For the FeS_2 sample, the dominant lattice fringes in high-resolution TEM (HRTEM) images (Figure 2b,c) have interplanar spacings of 0.2721 nm, corresponding to (200) planes.^[32] Figure 2f,g,j,k,n,o shows interplanar spacings of (200) planes are 0.2718, 0.2724, and 0.2730 nm for $\text{Fe}_{0.9}\text{Co}_{0.1}\text{S}_2$, $\text{Fe}_{0.75}\text{Co}_{0.25}\text{S}_2$ and $\text{Fe}_{0.5}\text{Co}_{0.5}\text{S}_2$, respectively. The selected area electron diffraction (SAED) patterns (Figure 2d,h) present clear-cut concentric circles with obvious bright spots, indicative of fairly good crystallinity for FeS_2 and $\text{Fe}_{0.9}\text{Co}_{0.1}\text{S}_2$. However, Figure 2l,p shows weakened diffraction spots with a strengthened ring-like shape in $\text{Fe}_{0.75}\text{Co}_{0.25}\text{S}_2$ and $\text{Fe}_{0.5}\text{Co}_{0.5}\text{S}_2$ samples, indicating polycrystalline characters caused by reduced APSs. The labeled diffraction rings are indexed as (111), (200), (210), (211), (220), (221), (311), and (222) planes of these samples, consistent with XRD refinement results. Moreover,

HAADF-STEM mapping results (Figure S4, Supporting Information) further confirm the homogenous element distribution of Fe, Co, and S in these samples.

The specific surface areas (SSAs) and pore size distributions for $\text{Fe}_{1-x}\text{Co}_x\text{S}_2$ ($x = 0, 0.1, 0.25, 0.5$) were characterized by N_2 adsorption/desorption as these properties play a crucial role in the battery performance.^[33] As seen in Figure S5 and Table S6 (Supporting Information), the Brunauer-Emmett-Teller (BET) SSAs of FeS_2 , $\text{Fe}_{0.9}\text{Co}_{0.1}\text{S}_2$, $\text{Fe}_{0.75}\text{Co}_{0.25}\text{S}_2$ and $\text{Fe}_{0.5}\text{Co}_{0.5}\text{S}_2$ are estimated to be 2, 5, 9 and 23 $\text{m}^2 \text{g}^{-1}$, respectively, as anticipated by the changes in particle sizes. Using the Barrett-Joyner-Halenda (BJH) method, FeS_2 shows pore size distribution (<20 nm) while pore size distributions (<12 nm) are seen for the $\text{Fe}_{0.9}\text{Co}_{0.1}\text{S}_2$, $\text{Fe}_{0.75}\text{Co}_{0.25}\text{S}_2$ and $\text{Fe}_{0.5}\text{Co}_{0.5}\text{S}_2$ samples. The thermal stability of $\text{Fe}_{1-x}\text{Co}_x\text{S}_2$ ($x = 0, 0.1, 0.25, 0.5$) samples was then investigated by thermal gravimetric (TGA) and differential scanning calorimetric (DSC) analyses (Figure S6, Supporting Information). TGA curves show a continuous mass loss with the increasing temperature. Apart from this, the DSC curves indicate that the decomposition temperature of FeS_2 under Ar (597 °C) is lower than those for $\text{Fe}_{0.9}\text{Co}_{0.1}\text{S}_2$, $\text{Fe}_{0.75}\text{Co}_{0.25}\text{S}_2$ and $\text{Fe}_{0.5}\text{Co}_{0.5}\text{S}_2$. $\text{Fe}_{0.5}\text{Co}_{0.5}\text{S}_2$ offers a somewhat higher thermal stability up to 631 °C. Thus, Co doping improves slightly the thermal stability of FeS_2 .

Previous measurements confirm that Co doping weakens M–S bonds and reduces APSs coincidentally with increasing SSAs. Raman spectra show that $\text{Fe}_{1-x}\text{Co}_x\text{S}_2$ ($x = 0, 0.1, 0.25, 0.5$) samples have similar bond structures (Figure 3a). Weak peaks

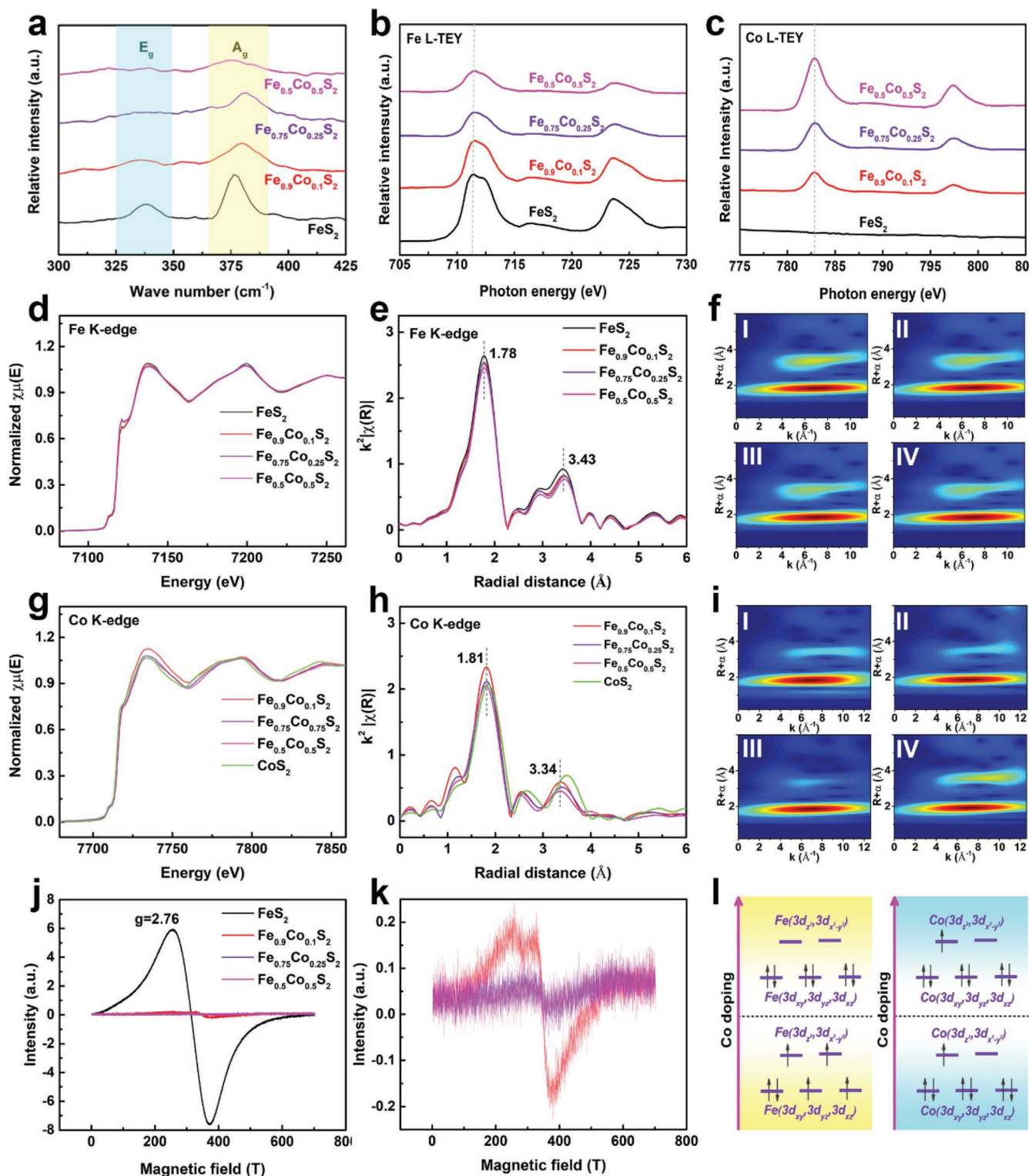


Figure 3. a) Raman spectra and sXAS spectra of as-prepared $\text{Fe}_{1-x}\text{Co}_x\text{S}_2$ ($x = 0, 0.1, 0.25, 0.5$) samples: b) Fe TEY, c) Co TEY modes. d) XANES spectra, e) FT-EXAFS, f) WT contour plots of Fe K-edge for (I) FeS_2 , (II) $\text{Fe}_{0.9}\text{Co}_{0.1}\text{S}_2$, (III) $\text{Fe}_{0.75}\text{Co}_{0.25}\text{S}_2$ and (IV) $\text{Fe}_{0.5}\text{Co}_{0.5}\text{S}_2$ samples. g) XANES spectra, h) FT-EXAFS, i) WT contour plots of Co K-edge for (I) $\text{Fe}_{0.9}\text{Co}_{0.1}\text{S}_2$, (II) $\text{Fe}_{0.75}\text{Co}_{0.25}\text{S}_2$, (III) $\text{Fe}_{0.5}\text{Co}_{0.5}\text{S}_2$ and (IV) CoS_2 samples. j, k) EPR spectra and locally enlarged area of as-prepared $\text{Fe}_{1-x}\text{Co}_x\text{S}_2$ ($x = 0, 0.1, 0.25, 0.5$) samples. l) Schematic diagram of d-electron regulations for Fe and Co atoms via the tuning effect caused by Co doping.

at $\approx 340\text{ cm}^{-1}$ most likely arise from the E_g vibration mode of S_2^{2-} dimer. Strong peaks at $\approx 380\text{ cm}^{-1}$ are related to the in-phase stretching vibration (A_g) of S_2^{2-} dimer.^[27] X-ray photoelectron spectra (XPS) was used to investigate the chemical compositions and valence states of $Fe_{1-x}Co_xS_2$ ($x = 0, 0.1, 0.25, 0.5$) samples. The low-resolution survey spectra (Figure S7a, Supporting Information) show that typical element signatures consist primarily of Fe, Co, and S. The Auger peaks of Co and Fe LMM will interfere with the peaks of Fe and Co 2p. In the high-resolution Fe 2p core level XPS spectra, depicted in Figure S7b (Supporting Information), the peaks of Fe $2p_{3/2}$ and Fe $2p_{1/2}$ coexist while the more intensive Fe $2p_{3/2}$ peak will be further analyzed for better accuracy. With the augment of Co doping ratio, the peak intensities of Fe $2p_{3/2}$ attenuate by degrees, suggestive of diminishing in Fe contents. However, the peak of Fe $2p_{3/2}$ at 707.1 eV for $Fe_{0.9}Co_{0.1}S_2$ shows a small blue shift compared with that of FeS_2 (707.0 eV).

As Co doping ratio increases, the locations of Fe $2p_{3/2}$ peaks remain at 707.1 eV for $Fe_{0.75}Co_{0.25}S_2$ and $Fe_{0.5}Co_{0.5}S_2$ samples, indicating that Co doping has little influence on the surface oxidation states of samples. Figure S7c (Supporting Information) displays the high-resolution Co 2p core level XPS spectra, with increasing peak intensities as Co doping ratio increases. The Co $2p_{3/2}$ peaks are centered at 779.2, 779.0, and 778.8 eV for $Fe_{0.9}Co_{0.1}S_2$, $Fe_{0.75}Co_{0.25}S_2$, and $Fe_{0.5}Co_{0.5}S_2$ samples, respectively, suggesting a decreasing oxidation state of sample surface, which is probably ascribed to that Co^{2+} ($3d^7$) holds a little higher d-electron charge density than Fe^{2+} ($3d^6$). In addition, the peaks of S $2p_{3/2}$ spectra (Figure S7d, Supporting Information) show slight blue shifts with Co doping. The S 2p peaks at 168.6 eV are pointed to S–O bonds in SO_x species.^[11b,34] All results imply that doping has little effect on the valence state of Fe, Co, and S, and Co may draw a little more electrons from S.

The electronic structures of samples were further probed using soft X-ray absorption spectroscopy (sXAS). A solid evolution of surface and bulk electronic structure could be explored by measuring in sXAS TEY and TFY modes with surface ($<10\text{ nm}$) and bulk ($>100\text{ nm}$) sensitivity, respectively.^[8a] As shown in Figure 3b,c, the Fe L-edge is divided into L2 (720 to 730 eV) and L3-edges (707 to 717 eV) and the Co L-edge is divided into L2 (792–802 eV) and L3-edges (778–788 eV), which originate from the $2p_{1/2}$ and $2p_{3/2}$ states due to the core–hole spin–orbital coupling.

The intensities for Fe-TEY and TFY (Figure S8a, Supporting Information) decrease gradually while those for Co-TEY and TFY (Figure S8b, Supporting Information) increase little by little, exhibiting an analogous trend. It implies that Fe and Co elements occupy evenly the Fe atom sites in the FeS_2 lattice. In addition, the peaks of Fe and Co L-edge in both TEY and TFY modes show no obvious shifts with increasing Co doping ratios. Thus, Co doping has little effect on the oxidation state of Fe and Co, consistent with XPS results.

Element-specific synchrotron radiation X-ray absorption fine structure (XAFS) measurements at the Fe and Co K-edge were also performed.^[35] Figures S9a and S10a (Supporting Information) show that Co K-edge XAFS spectra overlap partly the Fe K-edge XAFS spectra, further indicating successful Co doping. The Fe K-edge X-ray absorption near edge structure (XANES) spectra (Figure 3d) and the first derivative plots (Figure S9b,

Supporting Information) of $Fe_{1-x}Co_xS_2$ ($x = 0, 0.1, 0.25, 0.5$) are close to each other, indicating Co doping has little influence in the oxidation states of Fe. Moreover, Co K-edge XANES spectra (Figure 3g) of Co K-edge XANES for $Fe_{0.9}Co_{0.1}S_2$, $Fe_{0.75}Co_{0.25}S_2$, $Fe_{0.5}Co_{0.5}S_2$, and CoS_2 also show little changes when the Co doping ratio increases. However, the second peak in the first derivative plot (Figure S10b, Supporting Information) of CoS_2 is located at 7714.5 eV, lower than that of Co-doped FeS_2 (7715.7 eV), which is ascribed to the different interaction force between Fe–Co and Co–Co.

Figures S9c and S10c (Supporting Information) display the k^2 -weighted Fourier transformed (FT) plots of the extending X-ray absorption fine structure (EXAFS) shown in k -space for Fe and Co K-edges. The corresponding plots shown in R -space are displayed in Figure 3e,h. The prominent peaks at 1.78 Å in Fe K-edge spectra and 1.81 Å in Co K-edge spectra are attributed to Fe–S and Co–S coordination paths, respectively. Furthermore, Fe FT-EXAFS spectra (Figure 3e) show peaks centered at 3.43 Å, indicating the existence of Fe–Fe or Fe–Co coordination paths. Specifically, FT-EXAFS plots in R -space of Co-doped FeS_2 are similar without redundant peaks, inheriting the FeS_2 structure, which is also identified by fitting the FT-EXAFS curves of FeS_2 as displayed in Figure S11 and Table S7 (Supporting Information). The wavelet transformed (WT) contour plots (Figure 3f) for Fe K-edge of $Fe_{1-x}Co_xS_2$ ($x = 0, 0.1, 0.25, 0.5$) show two maximum intensity at 1.8 and 3.4 Å,^[36] which are assigned to the Fe–S and Fe–Fe/Fe–Co coordination paths. Besides, the intensities at 3.4 Å become a little weaker with increasing Co doping ratio. No other signals could be detected, demonstrating that Co doping does not change the surrounding bond structures of Fe atoms.

Co K-edge FT-EXAFS spectra in Figure 3h show peaks centered at 3.34 Å, indicating the Co–Fe or Co–Co coordination paths. Note that the peak for CoS_2 locates at the right side of peaks for $Fe_{0.9}Co_{0.1}S_2$, $Fe_{0.75}Co_{0.25}S_2$, and $Fe_{0.5}Co_{0.5}S_2$. The FT-EXAFS curves of CoS_2 shown in R -space were further fitted and the results (Figure S12 and Table S8, Supporting Information) matched well with experimental results, showing a similar crystal structure to FeS_2 . However, the obvious differences indicate that Co can occupy the Fe sites in the FeS_2 crystal lattice. The WT contour plots (Figure 3i) of $Fe_{0.9}Co_{0.1}S_2$, $Fe_{0.75}Co_{0.25}S_2$, $Fe_{0.5}Co_{0.5}S_2$, and CoS_2 show two maximum intensities at 1.8 and 3.3 Å, which is attributed to the Co–S and Co–Fe/Co–Co coordination paths. Simultaneously, the intensities at 3.3 Å get much weaker with increasing Co doping ratio. Nevertheless, the intensity of CoS_2 recovers to be strong. These results indicate that M–M ($M = Fe/Co$) interaction force weakens with increasing Co doping, which could be put down to the fact that adequate Co doping would make the FeS_2 lattice expand.

To investigate the electron distribution structures of atomic orbitals for Fe and Co, electron paramagnetic resonance (EPR) analysis was applied. Figure 3j,k shows that FeS_2 exhibits a significant signal with a g value of 2.76. Peak intensities varying with magnetic field decrease dramatically with enhanced Co contents. Interestingly, FeS_2 exhibits the strongest paramagnetism among all samples, probably ascribed to the high spin (HS) states of local Fe atoms with the 3d electronic configuration of $t_{2g}^4e_g^2$.^[30a] There can be two unpaired electrons in t_{2g} orbital and two unpaired electrons in e_g orbital (Figure 3l).

Thus, 10 at% Co doping can make HS states of Fe atoms to low spin (LS) states, resulting in an electronic configuration of $t^6_{2g}e^0_g$ without unpaired electrons. This inference is further confirmed when Co doping increases. Moreover, Co atoms in Co-doped FeS_2 should be in LS states with an electronic configuration of $t^6_{2g}e^1_g$, leaving one unpaired electron. Consequently, the local spin state modification by Co doping leads to a less e_g orbital electron filling for Fe atom while the spin state of Co atoms is little influenced.

2.2. The Mg^{2+} Storage Features of Co-Doped FeS_2 Cathodes for RMBs

The chemical structure of PMC electrolyte was first characterized by Fourier transform infrared reflection (FTIR) and Nuclear magnetic resonance (NMR), shown in Figure S13, Supporting Information. The active species in solution can be suggested to consist of cations of $[\text{Mg}_2(\mu\text{-Cl})_3\cdot 6\text{THF}]^+$ and anions of $[\text{Al}(\text{R-PhO})_{4-n}\text{Cl}_n]^-$ ($n = 1-4$).^[37] The electrochemical Mg stripping/plating behavior with prepared PMC electrolyte was investigated using cyclic voltammetry (CV) at 5 mV s^{-1} between -1 and 2 V . Figure S14a (Supporting Information) shows that the first reduction step begins at -0.6 V , which is ascribed to Mg plating on SS foils. In the subsequent oxidation step, the onset potential for Mg stripping from SS foils is 0 V . Then, the current density of cell increases sharply with an oxidation peak at 0.6 V . During subsequent cycles, the corresponding peak currents increase during Mg stripping/plating. The CV data illustrate clearly that PMC electrolyte enables reversible Mg stripping/plating. In addition, Figure S14b (Supporting Information) indicates that the oxidative stability of the electrolyte was calculated to be 3.25 V versus Mg^{2+}/Mg by linear sweep voltammetry (LSV) at 10 mV s^{-1} , which is suitable for our RMBs.

Figure S15 (Supporting Information) shows the Coulombic efficiency (CE) of Mg stripping/plating for the first 100 cycles in PMC electrolyte. The CE value is only 83.3% in the initial cycle, which is ascribed to some irreversible processes.^[7b] Then, CE gradually increases to 99.5% after 20 cycles and remains stable thereafter. The average CE for 100 cycles is 99.0%, which seems considerable for RMBs. Symmetric Mg cells were constructed to evaluate the performance in galvanostatic Mg stripping/plating measurements. Figure 4a and Figure S16a (Supporting Information) show that the polarization potential versus Mg^{2+}/Mg decreases gradually during initial cycles, suggestive of an activation process. Figure 4b indicates that the polarization potentials versus Mg^{2+}/Mg increase slightly with increasing current densities. The initial polarization potential is 78.5 mV (0.05 mA cm^{-2}), then increases to 105.5 mV (1 mA cm^{-2}), and recovers to 75 mV (0.05 mA cm^{-2}), indicating good rate performance for this electrolyte. The rapid decreasing over-potential is attributed to the deposition of a large amount of magnesium on electrode surface. Besides, Figure S16b (Supporting Information) shows that the polarization potential restabilizes at 32.9 mV after 240 cycles. Figure S17 (Supporting Information) demonstrates that PMC electrolyte endows symmetric cells with quite a low voltage hysteresis of 84.3 mV after cycling for 500 h, exhibiting considerable Mg stripping/plating kinetics and cycling stability.

The electrochemical performance of $\text{Fe}_{1-x}\text{Co}_x\text{S}_2$ ($x = 0, 0.1, 0.25, 0.5$) cathodes was investigated in CR2032 coin cells coupled with Mg anodes, PMC electrolyte and copper collectors. Figure 4c depicts the CV curves at 0.1 mV s^{-1} for initial three cycles of FeS_2 cathodes. During first discharge, a clear small peak at 0.9 V is ascribed to Mg^{2+} reaction with the FeS_2 cathode. However, as shown in Figure S18 (Supporting Information), similar peaks for Co-doped FeS_2 shift to lower voltages while the single peak of $\text{Fe}_{0.5}\text{Co}_{0.5}\text{S}_2$ splits into two peaks, indicating multi-step reactions. Then, the reduction peaks for all cathodes stabilize at 1.0 V during discharge. In the charging process, the anodic peaks show distinct characteristics where peaks (b, c, d) strengthen during cycling, indicating an apparent activation process and multistep oxidation. Particularly, the anodic peaks (a) turn to be more and more prominent with Co doping during later cycles. To fully clarify the electrochemical reaction after activation, CV curves (Figure 4d and Figure S18, Supporting Information) at 0.1 mV s^{-1} were obtained for the first three cycles when RMBs had cycled 50 times. Strong cathodic peaks (a') at 1.0 V are observed in $\text{Fe}_{1-x}\text{Co}_x\text{S}_2$ ($x = 0, 0.1, 0.25, 0.5$) cathodes. Moreover, the anodic peaks are significantly different. FeS_2 cathodes exhibit a broad polarization peak while Co-doped FeS_2 cathodes show three distinct peaks (b', c', d'), pointed to the multiple anodic reactions when Mg^{2+} is extracted from cathodes. Moreover, the overlap of CV curves proves the good reversibility of all cathode reactions.

As depicted in Figure 4e–h, $\text{Fe}_{1-x}\text{Co}_x\text{S}_2$ ($x = 0, 0.1, 0.25, 0.5$) cathodes show improved capacities during initial cycles with a CE of $>100\%$, based on the mass of Co-doped FeS_2 . On further cycling, the FeS_2 cathodes maintain a maximum discharge capacity of 700 mAh g^{-1} after 100 cycles. However, capacities decay gradually to 39 mAh g^{-1} after 200 cycles, which is probably ascribed to the FeS_2 electrode degradation caused by great volume change and irreversible reactions occurring in electrodes during discharge/charge.^[2,6b,38] The nanocrystallization of materials is an effective solution to this problem. The $\text{Fe}_{0.9}\text{Co}_{0.1}\text{S}_2$ cathodes show greatly improved performance, maintaining a highest discharge capacity of 661 mAh g^{-1} at 0.1 A g^{-1} after 106 cycles. Then, capacities show a downward trend after 170 cycles. $\text{Fe}_{0.75}\text{Co}_{0.25}\text{S}_2$ cathodes display a highest discharge capacity of 656 mAh g^{-1} after 91 cycles, maintaining a discharge capacity of 545 mAh g^{-1} after 200 cycles. These results indicate good capacity retention and enhanced electrode stability of the Co doping FeS_2 cathodes. $\text{Fe}_{0.5}\text{Co}_{0.5}\text{S}_2$ cathodes display a maximum capacity of 626 mAh g^{-1} after 62 cycles, showing the shortest activation process of 14 cycles among these four-type cathodes, and a reversible capacity of 613 mAh g^{-1} is obtained after 150 cycles. As a contrast, a previous study reported that a pyrite FeS_2 cathode coupled with $\text{Mg}[\text{B}(\text{hfp})_4]/\text{DME}$ electrolyte for RMB worked in a voltage range of $0.01-2.4 \text{ V}$ (vs Mg) but experienced serious overcharge during the 50th cycle,^[27] resulting in a short cycle life. These results indicate that Co-doped FeS_2 cathodes coupled with PMC electrolyte running in a narrower voltage window can retard the overcharge of batteries without reducing specific capacities, which is beneficial for improving the cycle life and stability of RMBs.

The cycling performance of Co-doped FeS_2 cathodes for RMBs was also investigated using the APC electrolyte. Figure S19 (Supporting Information) shows that FeS_2 and

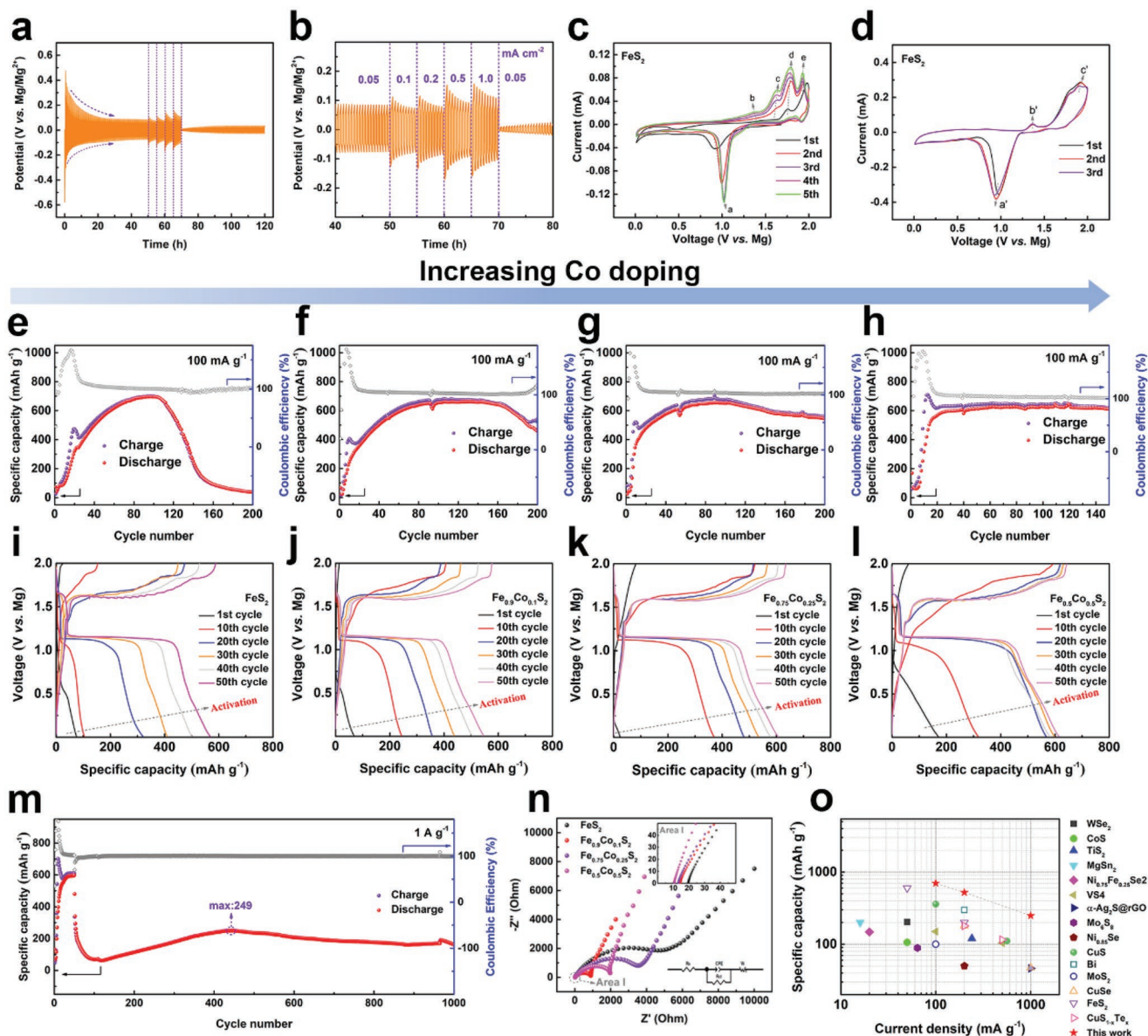


Figure 4. Cycling performance of symmetrical cells using PMC electrolyte at different current densities ($0.05\text{--}1\text{ mA cm}^{-2}$): a) 0 to 120 h and b) 40 to 60 h. The working, counter and reference electrodes of symmetrical cells are all Mg foils. CV at 0.1 mV s^{-1} for the first three cycles of c) pristine FeS_2 cathodes and d) cathodes having cycled 50 times at 0.1 A g^{-1} coupling with PMC electrolyte and copper collectors for RMBs. Cycling performance at 0.1 A g^{-1} of e) FeS_2 , f) $\text{Fe}_{0.9}\text{Co}_{0.1}\text{S}_2$, g) $\text{Fe}_{0.75}\text{Co}_{0.25}\text{S}_2$ and h) $\text{Fe}_{0.5}\text{Co}_{0.5}\text{S}_2$ cathodes for RMBs. The corresponding discharge/charge profiles during 1st, 10th, 20th, 30th, 40th and 50th cycles for i) FeS_2 , j) $\text{Fe}_{0.9}\text{Co}_{0.1}\text{S}_2$, k) $\text{Fe}_{0.75}\text{Co}_{0.25}\text{S}_2$ and l) $\text{Fe}_{0.5}\text{Co}_{0.5}\text{S}_2$ cathodes. m) Cycling performance at 1 A g^{-1} of $\text{Fe}_{0.5}\text{Co}_{0.5}\text{S}_2$ cathodes for RMBs after 50 cycles at 0.1 A g^{-1} . n) EIS of $\text{Fe}_{1-x}\text{Co}_x\text{S}_2$ ($x = 0, 0.1, 0.25, 0.5$) cathodes for RMBs, and inset is enlarged image of low impedance. o) Electrochemical performance comparison of Co-doped FeS_2 cathodes with other typical cathode materials for RMBs reported in the literature.

$\text{Fe}_{0.5}\text{Co}_{0.5}\text{S}_2$ cathodes coupled with APC electrolyte show much lower discharge capacities and longer activation time than those using PMC electrolyte, likely a result of the greater nucleophilicity of APC electrolyte. Additionally, commercial CoS_2 was characterized by XRD and SEM (Figure S20a,b, Supporting Information), then used for RMBs. Figure S20c,d (Supporting Information) indicates that CoS_2 cathodes show increasing capacities during cycling with long activation time.

The results indicate that Co doping improves the significantly electrochemical performance of FeS_2 . On the one side, APSs decrease sharply with enhanced SSAs for Co-doped FeS_2 ,

benefiting electrolyte infiltration into the electrode materials. Co doping likely weakens M–S ($M = \text{Fe}, \text{Co}$) bond strengths, beneficial to the transformation from M–S ($M = \text{Fe}, \text{Co}$) to Mg–S and the whole reversible reactions during RMB cycling. Moreover, the local spin state of FeS_2 could be modified by Co doping, resulting in a less e_g orbital electron filling in Co-doped FeS_2 . These adjustable and stable states could be one potential reason for reversible and stable RMBs. Moreover, the synergistic catalytic effect of Fe and Co can also improve the performance. Figure 4i–l exhibits discharge/charge curves of $\text{Fe}_{1-x}\text{Co}_x\text{S}_2$ ($x = 0, 0.1, 0.25, 0.5$) cathodes at 0.1 A g^{-1} , showing

a clear activation process. Besides, all cathodes exhibit long discharge plateaus at 1.15 V after battery activation, implying a similar Mg^{2+} storage process during battery discharging.

$\text{Fe}_{1-x}\text{Co}_x\text{S}_2$ ($x = 0, 0.1, 0.25, 0.5$) cathodes were also cycled from 0.1 to 1 A g^{-1} as seen in Figure S21 (Supporting Information), which displays rate performance of RMBs and corresponding discharge/charge curves. All cathodes display decreasing capacities with increasing current densities. It should be noted that the capacities present a descending trend at every current density without stabilizing. Therefore, all cathodes were cycled at 1 A g^{-1} where cathodes were preactivated 50 cycles at 0.1 A g^{-1} . Figure S22 (Supporting Information) shows that capacities of all cathodes decrease sharply starting at 1 A g^{-1} , followed by slow rising. FeS_2 cathodes show unstable capacities in cycles 340–500 where a maximum capacity of 374 mAh g^{-1} is obtained, probably due to the huge volume expansion and contraction of cathode materials.^[6b,27] In contrast, $\text{Fe}_{0.9}\text{Co}_{0.1}\text{S}_2$ cathodes show steadier capacities with a discharge capacity of 157 mAh g^{-1} after 340 cycles. $\text{Fe}_{0.75}\text{Co}_{0.25}\text{S}_2$ cathodes show a capacity of 161 mAh g^{-1} after 450 cycles, suggesting that Co doping can improve the RMB stability at high current densities. Even better, $\text{Fe}_{0.5}\text{Co}_{0.5}\text{S}_2$ cathodes (also Figure 4m) show a maximum capacity of 250 mAh g^{-1} after 440 cycles and maintain a capacity of 164 mAh g^{-1} after 1000 cycles, displaying the best cycling stability among these four samples.

Electrochemical impedance spectroscopy (EIS) measurement was performed. Figure 4n compares the Nyquist plots of $\text{Fe}_{1-x}\text{Co}_x\text{S}_2$ ($x = 0, 0.1, 0.25, 0.5$) cathodes for RMBs. As depicted, $\text{Fe}_{0.9}\text{Co}_{0.1}\text{S}_2$ cathode displays a reduced charge transfer resistance (R_{ct}) of $\approx 890 \Omega$, lower than those of FeS_2 ($\approx 4600 \Omega$), $\text{Fe}_{0.75}\text{Co}_{0.25}\text{S}_2$ ($\approx 3800 \Omega$), and $\text{Fe}_{0.5}\text{Co}_{0.5}\text{S}_2$ ($\approx 2000 \Omega$) cathodes. The resistance of whole cell components (denoted as R_s) is a combination of the electrolyte-accessible area, electrical conductivity of the electrode and solid electrolyte interface. Moreover, R_s of $\text{Fe}_{0.5}\text{Co}_{0.5}\text{S}_2$ (10 Ω) is lower than those of FeS_2 (20 Ω), $\text{Fe}_{0.9}\text{Co}_{0.1}\text{S}_2$ (15 Ω), and $\text{Fe}_{0.75}\text{Co}_{0.25}\text{S}_2$ (13 Ω).

Overall, the electrochemical performance of Co-doped FeS_2 cathodes for RMBs is comparable with other RMBs reported before (Figure 4o and Table S3, Supporting Information).^[5a,9c,21,22d,25,27,39] In addition, in this study, inexpensive PMC electrolyte and Co-doped FeS_2 cathodes are applied for high-performance RMBs, showing great potential of applying such RMBs in energy storage fields.

2.3. The Mg^{2+} Storage Mechanisms of RMBs

Mg^{2+} storage behavior was investigated via various measurements. Operando synchrotron X-ray diffraction (SXRD) shed light on the structural evolution of FeS_2 and $\text{Fe}_{0.5}\text{Co}_{0.5}\text{S}_2$ cathodes for RMBs during initial cycles at 0.1 A g^{-1} . For these tests, the pre-drilled positive/negative shells were covered with Kapton films to facilitate the transmission of synchrotron radiation light as shown in Figure 5a. The voltage-time curves for the FeS_2 cathodes during initial cycles and corresponding operando SXRD patterns are shown in Figure S23 (Supporting Information). The as-fabricated electrode unveils the typical diffraction peaks corresponding to crystalline planes of FeS_2 (JCPDS no. 71-0053). The intense diffraction peaks of the copper collector

are also presented. The diffraction peaks for FeS_2 appear during later discharge-charge-discharge, indicating inadequate Mg^{2+} reaction with FeS_2 cathode.

However, operando SXRD patterns of $\text{Fe}_{0.5}\text{Co}_{0.5}\text{S}_2$ cathode during initial cycles, represented in Figure S24 (Supporting Information), show some different phenomena from those of FeS_2 cathode. Diffraction peaks matching well with those of $\text{Fe}_{0.5}\text{Co}_{0.5}\text{S}_2$ are also found. In the meanwhile, the diffraction peaks for $\text{Cu}_{1.8}\text{S}$ and S were detected during cycling, suggesting that $\text{Fe}_{0.5}\text{Co}_{0.5}\text{S}_2$ reacts partially with copper collector. The preferred reaction of $\text{Fe}_{0.5}\text{Co}_{0.5}\text{S}_2$ than FeS_2 with Cu can arise owing to the smaller particle sizes and longer M–S (M = Fe and Co) bond lengths, reducing the energetic requirements of the reaction path and resulting in a shorter-term activation time for RMBs.

To investigate the reaction behavior of FeS_2 cathode during the 50th cycle at 0.1 A g^{-1} , operando SXRD was further performed to disclose the concrete reaction processes after cell activation. First, CR2032 cells using FeS_2 cathodes were disassembled. Then, the cathodes and separators were transferred to new cell cases. Ample electrolyte and polished Mg foils were replenished. The cells for operando SXRD experiments were then assembled. Figure 5b shows that new peaks for MgS exist during 50th discharge/charge, indicating that partially irreversible MgS conversion causes deviations between theoretical and actual specific capacity for FeS_2 cathode. Furthermore, Figure 5c presents a closer look at the variation of MgS (200) peak, showing gradual increasing intensities during discharge accompanied by a declining trend during charge. The diffraction peaks of (211) planes for Fe are also detected. It is salient that the dominant cathode reactions after cell activation differentiate from those during initial cycling.

Concurrently, ex situ XPS was employed to identify the chemical compositions and valence states during the 50th cycle at 0.1 A g^{-1} for FeS_2 and $\text{Fe}_{0.5}\text{Co}_{0.5}\text{S}_2$ cathodes from dismantled RMBs, emphasizing Fe 2p, Co 2p, Cu 2p, S 2p, and Mg 2p spectra. For FeS_2 cathodes, six states (state I–VI) were chosen as presented in Figure S25a (Supporting Information). Figure 5d shows that the Mg 2p peaks shift to lower binding energy during discharge (state I to IV) with increasing intensities and move back after charge (state V, VI), suggesting the reversible reaction of Mg^{2+} with cathodes.^[8a,11b,39h] The Cu 2p spectra (Figure S25b, Supporting Information) show obvious changes during cycling, where Cu^0 is found in the fully discharged state (state IV) and Cu^+ is detected in fully charged state (state I, VI).^[10,22a,25]

In a striking contrast, the Fe 2p spectra (Figure S25c, Supporting Information) do not change conspicuously during discharge/charge, demonstrating that most Fe species may not participate in the conversion reactions during cycling when the cell is fully activated. Moreover, the S 2p peaks (Figure 5e) also shift to a lower energy region during discharge and shift to a higher energy region during charge. The peaks of Mg–S strengthen greatly while the peaks of Cu–S weaken apparently during discharge. Then, the peaks of Mg–S weaken gradually while the peaks of Cu–S strengthen by degrees during charge, which is probably assigned to the mutual transformation between Cu–S and Mg–S species. XPS of the cathode surface also eliminates the influence of the copper collector. These results further confirm that the conversion reaction of Mg^{2+}

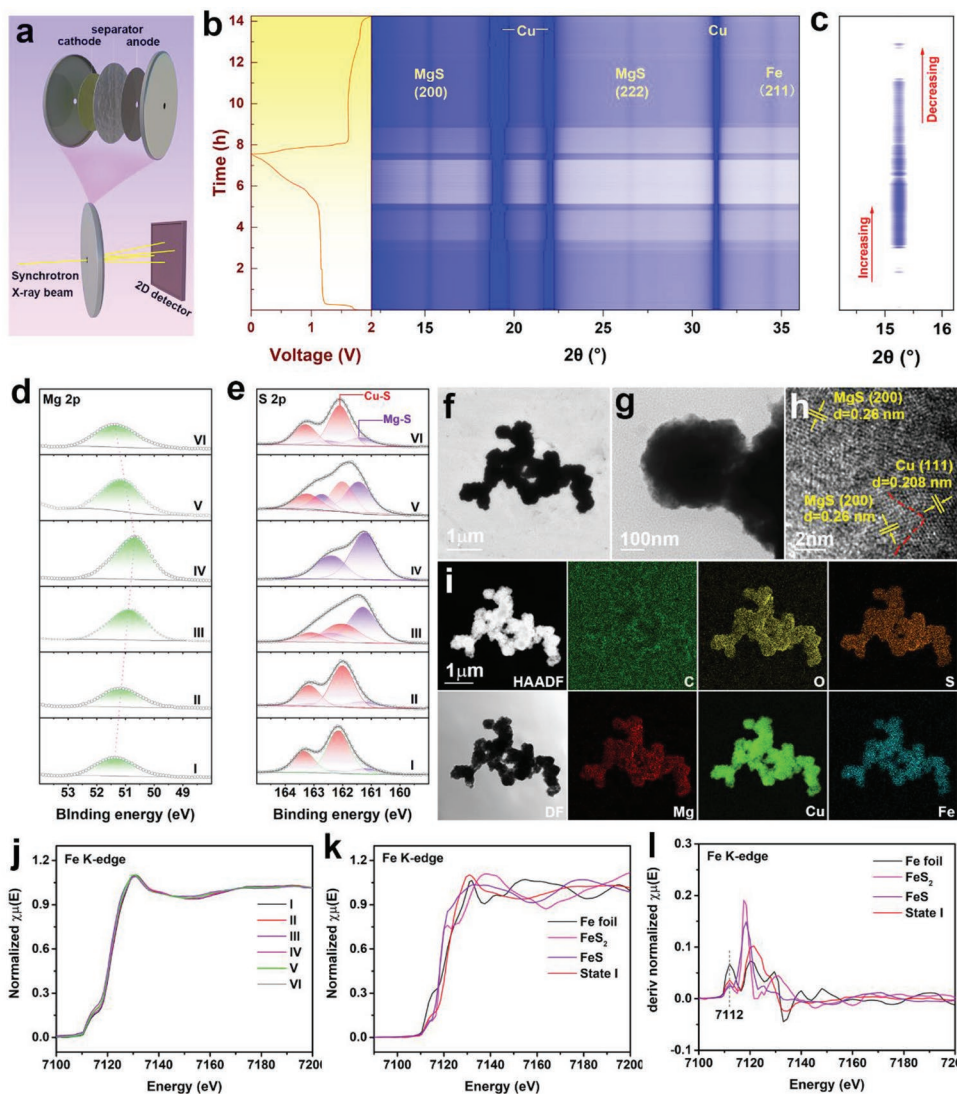


Figure 5. a) Schematic diagram of operando SXR tests for RMBs. b) The voltage-time curve of FeS_2 cathodes coupling with PMC electrolyte and copper collectors during 50th cycle and corresponding contour plots of operando SXR patterns. c) Counter plots of partial operando SXR. d) Mg 2p and e) S 2p spectra of FeS_2 cathodes in different states (I–VI). f, g) TEM image, h) HRTEM images, i) HAADF, DF images and corresponding STEM mapping results of FeS_2 cathode in fully discharged state (cycle 50). j) Fe K-edge XANES spectra of FeS_2 cathodes in different states. k) Fe K-edge XANES spectra and l) the first derivative plots for FeS_2 , FeS, Fe foil, and FeS_2 cathodes (state I).

with $\text{Cu}_{1.8}\text{S}$ to produce Cu and MgS should contribute to the capacities of our cells after activation, rather than the conversion reactions from Fe–S species to MgS.

As for $\text{Fe}_{0.5}\text{Co}_{0.5}\text{S}_2$ cathodes during 50th cycle, six states (Figure S26a, Supporting Information) were chosen and the ex situ XPS analyses give similar conclusions. The peaks of Fe and Co 2p spectra (Figure S26b,c, Supporting Information) show no obvious shifts during discharge/charge, also indicating that Fe and Co species may not participate in the conversion reactions. However, the peaks of Cu 2p spectra (Figure S26d, Supporting Information) for cathodes in a fully charged state (state I, VI) are at lower binding energies than those for cathodes in a fully discharged state (state IV), showing that the reversible reaction “ $\text{Cu}_{1.8}\text{S} + \text{Mg}^{2+} \leftrightarrow \text{Cu} + \text{MgS}$ ” also contributes to the capacities of $\text{Fe}_{0.5}\text{Co}_{0.5}\text{S}_2$ cathodes after activation.

In addition, the peak intensities of Mg 2p spectra (Figure S26e, Supporting Information) increase after discharge, indicating successful Mg^{2+} storage in the cathodes. Simultaneously, peaks of S 2p spectra (Figure S26f, Supporting Information) verify the mutual transformation between Cu–S and Mg–S species. Overall, after long-term cycling, the discharge capacities of cells derive mainly from the generation of Cu and MgS. No obvious change in the valence states of Fe and Co species indicates that they may take catalytic effects for facilitating the reversible conversion for Cu–S species.

Figure S27a,b (Supporting Information) present SEM images of pristine FeS_2 cathode. The corresponding EDX results (Figure S27c–h and Table S9, Supporting Information) show that a low Cu content of 1.8 wt% was detected. Moreover, Figures S28, S29 and Table S9 (Supporting Information)

show that Mg/S mass ratio changes considerably from 81.3 to 30.7% during the 50th discharge/charge. However, considerable amounts of Cu are detected on the cathode surface while the Fe content is as low as 0.6 wt% after 50 cycles. For the pristine Fe_{0.5}Co_{0.5}S₂ cathode, Figure S30 and Table S10 (Supporting Information) show a comparatively high Cu content of 13.5 wt%, indicating that Fe_{0.5}Co_{0.5}S₂ tends to react easily with the copper collector as proved in operando SXRD. Figures S31, S32 and Table S10 (Supporting Information) exhibit the low contents of Fe and Co in the cathode after 50 cycles while the content of Cu is high. Simultaneously, the Mg/S mass ratio also shows an obvious decrease during the 50th discharge/charge. These results demonstrate that the Cu species participate eventually in the process of Mg²⁺ storage for FeS₂ and Fe_{0.5}Co_{0.5}S₂ cathodes after battery activation.

TEM analyses were also performed to determine the cathode product phases in FeS₂ cathode after 50 cycles. After full discharge, TEM images in Figure 5f,g show the products consists of aggregated particles. The dominant lattice fringes in HRTEM image (Figure 5h) have interplanar spacings of 0.26 and 0.208 nm, corresponding to the (200) planes of MgS and (111) planes of Cu, respectively. Figure 5i shows the HAADF, DF images of the product, and STEM mapping results demonstrate a focused homogeneous element distribution. In addition, Figure S33a,b (Supporting Information) shows the

morphologies of products after charge. HRTEM (Figure S33c,d, Supporting Information) images indicate that Cu_{1.8}S and Cu coexist coincident with Fe and FeS.

To understand the role of Fe and Co more accurately during cycling, the valence states of the Fe, Co species in FeS₂ and Fe_{0.5}Co_{0.5}S₂ cathodes were also deciphered via XANES spectra. It is found that Fe K-edge spectra (Figure 5j) show little changes during discharge/charge. Figure 5k,l shows that Fe K-edge XANES spectrum for FeS₂ cathode during 50th cycle at state I is situated between those for Fe foil and FeS, not close to that for FeS₂. Moreover, there are two obvious peaks at 7112 and 7120 eV in the first derivative plots (Figure S34, Supporting Information), which can be ascribed to Fe⁰ and iron sulfides like FeS, indicating a mixture of Fe and Fe–S species in the cathode during cycling.

For Fe_{0.5}Co_{0.5}S₂ cathodes, Fe and Co (Figures S35, S36, Supporting Information) K-edge XANES spectra also show little change during discharge/charge, which further confirms the catalytic effect of Fe and Co species. Overall, the valence state of Fe, Co elements in cathodes shows little change during cycling, demonstrating a catalytic effect rather than acting as Mg²⁺ carriers.

The Mg²⁺ storage mechanisms for FeS₂ and Co-doped FeS₂ cathodes can be schematically summarized in Figure 6. Primarily, Co doping can reduce APSs and enhance particle

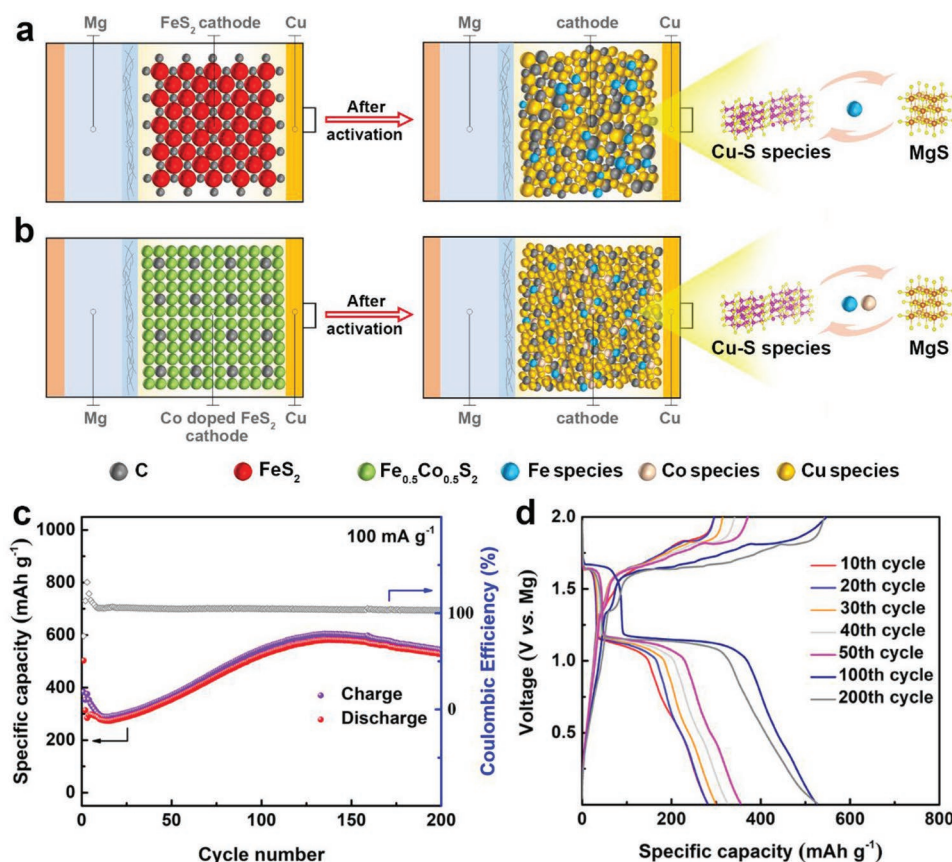


Figure 6. Schematic diagrams of RMBs working during initial cycles and after activation using a) FeS₂ cathodes and b) Fe_{0.5}Co_{0.5}S₂ cathodes. c) Cycling performance at 0.1 A g⁻¹ and d) corresponding discharge/charge profiles during 10th, 20th, 30th, 40th, 50th, 100th and 200th cycles of sulfur cathodes for RMBs using PMC electrolyte and copper collectors.

SSAs, favoring the generation of Cu-S species like $\text{Cu}_{1.8}\text{S}$ and accelerating battery activation. After full activation, Figure 6a shows that reversible conversion of Cu-S species to MgS dominates FeS_2 cathode reactions where Fe species can improve the reaction kinetics. Figure 6b shows that Fe and Co species enhance synergistically kinetics for the reversible conversion of Cu-S species to MgS. Besides, the Cu species like Cu and $\text{Cu}_{1.8}\text{S}$ can interpenetrate in the cathodes, forming continuous and advantageous electronic pathways.

Figure S18b,d,f,h (Supporting Information) show the electrochemical reactions for all cathodes after activation. Strong cathodic peaks (a') are observed in all cathodes for RMBs, ascribed to the conversion of Cu-S species to Cu. The anodic peaks are pointed to the multiple anodic reactions. Furthermore, Figure S37 (Supporting Information) shows that the redox reaction over-potential for $\text{Fe}_{0.5}\text{Co}_{0.5}\text{S}_2$ is smaller than FeS_2 , $\text{Fe}_{0.9}\text{Co}_{0.1}\text{S}_2$, and $\text{Fe}_{0.75}\text{Co}_{0.25}\text{S}_2$ at 0.1 A g^{-1} after 30 cycles. After 50 cycles, analogic voltage differentiation is observed in all electrodes. This implies that Co doping is beneficial to the reversible conversion reactions of electrode materials during initial cycles, suggestive of a more effective catalytic effect for cathode conversion reactions.

The electrochemical kinetics of FeS_2 and $\text{Fe}_{0.5}\text{Co}_{0.5}\text{S}_2$ cathodes for RMBs using PMC electrolyte were studied via EIS measurements after 10, 30, 50, and 150 cycles at 0.1 A g^{-1} (Figure S38, Supporting Information). R_{ct} decreases gradually for both FeS_2 and $\text{Fe}_{0.5}\text{Co}_{0.5}\text{S}_2$ cathodes and the slope of straight line increases gradually during the first 50 cycles, which is ascribed to the improved reaction kinetics at the electrodes and enhanced Mg^{2+} diffusion rates during battery activation.^[40] R_{ct} for FeS_2 cathodes increases to $\approx 5000 \Omega$ while R_{ct} for $\text{Fe}_{0.5}\text{Co}_{0.5}\text{S}_2$ cathodes remains at $\approx 100 \Omega$ after 150 cycles. Moreover, R_s of FeS_2 cathodes increases from 16Ω (50th cycle) to 58Ω (150th cycles) while R_s of $\text{Fe}_{0.5}\text{Co}_{0.5}\text{S}_2$ cathodes is stable at 31Ω after 150 cycles. These results show that $\text{Fe}_{0.5}\text{Co}_{0.5}\text{S}_2$ cathodes have better electrochemical kinetic performance than FeS_2 cathodes after long-term cycling, demonstrating the advantages of Co doping strategy.

Inspired by the success in the realization of high-performance RMBs using Co-doped FeS_2 cathodes and copper collector, this strategy was extended to typical sulfur cathodes. Figure 6c,d indicate that sulfur cathodes show increasing capacities up to 583 mAh g^{-1} at 0.1 A g^{-1} after 138 cycles. A discharge plateau at 1.66 V is observed, probably ascribed to the conversion of S to magnesium polysulfide (MgS_x).^[12] Particularly, the second discharge plateau at 1.15 V resembles those of Co-doped cathodes for RMBs, possibly assigned to the conversion of Cu-S species to MgS. Besides, at 1 A g^{-1} , sulfur cathodes show a reversible discharge capacity of 236 mAh g^{-1} after 800 cycles, as presented in Figure S39 (Supporting Information). It is obvious that sulfur cathodes for RMBs have longer activation time than Co-doped FeS_2 cathodes, further confirming the catalytic effect of Fe and Co in accelerating battery activation.

Overall, the rate of reaction between cathode and copper collector to form Cu-S species like $\text{Cu}_{1.8}\text{S}$ determines the overall activation time for these types of RMBs. Co doping can be an effective strategy to accelerate the activation. In light of the fact that FeS_2 is easily decomposed to Fe and S in inert atmosphere at high temperatures, a preactivation method uses charging at con-

stant voltage providing electric energy to replace thermal energy. Herein, $\text{Fe}_{0.5}\text{Co}_{0.5}\text{S}_2$ cathodes were selected for RMBs, then charged directly to 2 V and kept for different time. Figure S40 (Supporting Information) shows that the preactivation strategy further shortens the activation time. Moreover, the $\text{Fe}_{0.5}\text{Co}_{0.5}\text{S}_2$ cathodes after pre-charging for 2 h show the activation time of 9 cycles with a CE of 108% after 120 cycles. Nevertheless, the CE is higher than 100%, increasing as precharging time increases. Generally, the possibly formed elemental S can not only react easily with Cu but also participate in the cathode reactions, further accelerating the battery activation. The shuttle effect caused by generated MgS_x may account for the serious overcharging of these RMBs. However, the reaction mechanism is worthy of further exploration, although not within the scope of this study.

3. Conclusions

A simple hydrothermal method was successfully utilized to synthesize $\text{Fe}_{1-x}\text{Co}_x\text{S}_2$ ($x = 0, 0.1, 0.25, 0.5$) materials. XRD Rietveld refinement results with assistance of HRTEM observations confirm that Co doping can make the M-S bond ($M = \text{Fe/Co}$) lengthen. Simultaneously, the particle size is greatly dwindling and the specific surface area is gradually increasing with the increase in Co doping ratio. Thus, Co doping can be highly advantageous for improving the electrochemical performance of RMBs. Intensive spectroscopic experiments like XPS, XAS, XAFS, and EPR were further employed to comprehend deeply the electron structures. In detail, the tuning effect by Co doping can make the *d*-electron distribution of Fe from $t_{2g}^4 e_g^2$ (HS state) to $t_{2g}^6 e_g^0$ (LS state), reducing the paramagnetism of samples. The electronic configuration of Co is not influenced, indicative of the mutual interaction between Fe and Co. Later experimental results confirm the improved synergetic catalytic effect induced by Fe and Co species for RMBs.

A non-nucleophilic PMC electrolyte was rationally coupled with Co-doped cathodes and copper collector for RMBs, displaying good electrochemical performance. Even though Co doping can reduce slightly the capacity, the activation time of Co-doped FeS_2 cathodes is obviously shortened compared with FeS_2 cathodes. Particularly, $\text{Fe}_{0.5}\text{Co}_{0.5}\text{S}_2$ cathodes show a high capacity of 613 mAh g^{-1} over 150 cycles at 0.1 A g^{-1} and even maintain 164 mAh g^{-1} over 1000 cycles at 1 A g^{-1} . Operando SXR results show that FeS_2 cathode is stable during initial cycling. Besides, the more inclination to form Cu-S species like $\text{Cu}_{1.8}\text{S}$ can account for the shorter activation time of $\text{Fe}_{0.5}\text{Co}_{0.5}\text{S}_2$ cathodes. Importantly, the results of operando SXR, XPS, XANES, TEM, SEM and EDX indicate that the capacity is mainly contributed by the Mg reaction with $\text{Cu}_{1.8}\text{S}$ after battery activation while Fe and Co species take actions with a synergistic catalytic effect. Thus, this work may remind us that we should pay adequate attention to the electrochemical behaviors of Cu when chalcogenide materials coated on copper collector are used for kinds of batteries. Moreover, this study demonstrates that the usage of PMC electrolyte and doping strategy could be well applied for high-performance RMBs.

Supporting Information

Supporting Information is available from the Wiley Online Library or from the author.

Acknowledgements

The authors thank the staff at Beamline (BL02B02, BL11B, BL14B1, and BL15U) of the Shanghai Synchrotron Radiation Facility. H.X. thanks the supporting from “Zhiyuan Honor Program” for doctoral students, Shanghai Jiao Tong University. This work was supported by the National Natural Science Foundation of China (No.52171186), the Science and Technology Commission of Shanghai Municipality (CN) under No.19511108100, Shanghai Education Commission “Shuguang” scholar project (CN, 16SG08) and the funding from Center of Hydrogen Science, Shanghai Jiao Tong University. The authors also appreciate the support from the Instrumental Analysis Center, Shanghai Jiao Tong University.

Conflict of Interest

The authors declare no conflict of interest.

Data Availability Statement

The data that support the findings of this study are available from the corresponding author upon reasonable request.

Keywords

Co doping, FeS₂ cathodes, non-nucleophilic electrolytes, rechargeable magnesium batteries, synchrotron radiation spectroscopy

Received: May 11, 2022

Revised: July 30, 2022

Published online: August 21, 2022

- [1] a) R. Mohtadi, O. Tutusaus, T. S. Arthur, Z. Zhao-Karger, M. Fichtner, *Joule* **2021**, 5, 581; b) I. D. Johnson, B. J. Ingram, J. Cabana, *ACS Energy Lett.* **2021**, 6, 1892.
- [2] M. Mao, T. Gao, S. Hou, C. Wang, *Chem. Soc. Rev.* **2018**, 47, 8804.
- [3] a) B. L. Mordike, T. Ebert, *Mater. Sci. Eng. A* **2001**, 302, 37; b) W. Zhu, L. Ren, C. Lu, H. Xu, F. Sun, Z. Ma, J. Zou, *ACS Nano* **2021**, 15, 18494.
- [4] Y. Wang, H. Huang, G. Jia, H. Zeng, G. Yuan, *Acta Biomater.* **2021**, 135, 705.
- [5] a) D. Aurbach, Z. Lu, A. Schechter, Y. Gofer, H. Gizbar, R. Turgeman, Y. Cohen, M. Moshkovich, E. Levi, *Nature* **2000**, 407, 724; b) J. Muldoon, C. B. Bucur, T. Gregory, *Chem. Rev.* **2014**, 114, 11683; c) J. Song, E. Sahadeo, M. Noked, S. B. Lee, *J. Phys. Chem. Lett.* **2016**, 7, 1736.
- [6] a) H. Shuai, J. Xu, K. Huang, *Coord. Chem. Rev.* **2020**, 422, 213478; b) M. D. Regulacio, D. T. Nguyen, R. Horia, Z. W. Seh, *Small* **2021**, 17, 2007683.
- [7] a) M. Matsui, *J. Power Sources* **2011**, 196, 7048; b) Y. Li, S. Guan, H. Huo, Y. Ma, Y. Gao, P. Zuo, G. Yin, *Adv. Funct. Mater.* **2021**, 31, 2100650; c) S. G. McArthur, L. Geng, J. Guo, V. Lavallo, *Inorg. Chem. Front.* **2015**, 2, 1101.
- [8] a) H. Xu, X. Zhang, T. Xie, Z. Li, F. Sun, N. Zhang, H. Chen, Y. Zhu, X. Zou, C. Lu, J. Zou, R. M. Laine, *Energy Storage Mater.* **2022**, 46, 583; b) K. Shimokawa, T. Atsumi, N. L. Okamoto, T. Kawaguchi, S. Imashuku, K. Wagatsuma, M. Nakayama, K. Kanamura, T. Ichitsubo, *Adv. Mater.* **2021**, 33, 2007539.
- [9] a) L. F. Wan, D. Prendergast, *J. Am. Chem. Soc.* **2014**, 136, 14456; b) S. Hou, X. Ji, K. Gaskell, P. Wang, L. Wang, J. Xu, R. Sun, O. Borodin, C. Wang, *Science* **2021**, 374, 172; c) H. D. Yoo, Y. Liang, H. Dong, J. Lin, H. Wang, Y. Liu, L. Ma, T. Wu, Y. Li, Q. Ru, Y. Jing, Q. An, W. Zhou, J. Guo, J. Lu, S. T. Pantelides, X. Qian, Y. Yao, *Nat. Commun.* **2017**, 8, 339.
- [10] C. Pei, F. Xiong, Y. Yin, Z. Liu, H. Tang, R. Sun, Q. An, L. Mai, *Small* **2021**, 17, 2004108.
- [11] a) L. Li, H. Chen, E. He, L. Wang, T. Ye, J. Lu, Y. Jiao, J. Wang, R. Gao, H. Peng, Y. Zhang, *Angew. Chem., Int. Ed.* **2021**, 60, 15317; b) H. Xu, D. Zhu, W. Zhu, F. Sun, J. Zou, R. M. Laine, W. Ding, *Chem. Eng. J.* **2022**, 428, 131031; c) Z. Zhang, B. Chen, H. Xu, Z. Cui, S. Dong, A. Du, J. Ma, Q. Wang, X. Zhou, G. Cui, *Adv. Funct. Mater.* **2018**, 28, 1701718; d) T. Lu, Z. Zhang, B. Chen, S. Dong, C. Wang, A. Du, L. Wang, J. Ma, G. Cui, *Mater. Today Energy* **2020**, 17, 100450.
- [12] H. S. Kim, T. S. Arthur, G. D. Allred, J. Zajicek, J. G. Newman, A. E. Rodnyansky, A. G. Oliver, W. C. Boggess, J. Muldoon, *Nat. Commun.* **2011**, 2, 427.
- [13] a) J. Muldoon, C. B. Bucur, A. G. Oliver, T. Sugimoto, M. Matsui, H. S. Kim, G. D. Allred, J. Zajicek, Y. Kotani, *Energy Environ. Sci.* **2012**, 5, 5941; b) Z. Zhirong, F. Maximilian, *MRS Commun.* **2017**, 7, 770.
- [14] R. K. Bhardwaj, A. J. Bhattacharyya, *ACS Appl. Energy Mater.* **2021**, 4, 14121.
- [15] O. Tutusaus, R. Mohtadi, T. S. Arthur, F. Mizuno, E. G. Nelson, Y. V. Sevryugina, *Angew. Chem., Int. Ed.* **2015**, 54, 7900.
- [16] R. Jay, A. W. Tomich, J. Zhang, Y. Zhao, A. De Gorostiza, V. Lavallo, J. Guo, *ACS Appl. Mater. Interfaces* **2019**, 11, 11414.
- [17] K. Itaoka, I.-T. Kim, K. Yamabuki, N. Yoshimoto, H. Tsutsumi, *J. Power Sources* **2015**, 297, 323.
- [18] Z. Zhao-Karger, R. Liu, W. Dai, Z. Li, T. Diemant, B. P. Vinayan, C. B. Minella, X. Yu, A. Manthiram, R. J. Behm, M. Ruben, M. Fichtner, *ACS Energy Lett.* **2018**, 3, 2005.
- [19] a) Y. Ji, X. Liu-Théato, Y. Xiu, S. Indris, C. Njel, J. Maibach, H. Ehrenberg, M. Fichtner, Z. Zhao-Karger, *Adv. Funct. Mater.* **2021**, 31, 2100868; b) Y. Xu, W. Li, G. Zhou, Z. Pan, Y. Zhang, *Energy Storage Mater.* **2018**, 14, 253; c) W. Wang, H. Yuan, Y. NuLi, J. Zhou, J. Yang, J. Wang, *J. Phys. Chem. C* **2018**, 122, 26764.
- [20] F. Liu, T. Wang, X. Liu, L. Z. Fan, *Adv. Energy Mater.* **2020**, 11, 2000787.
- [21] a) X. Xu, D. Chao, B. Chen, P. Liang, H. Li, F. Xie, K. Davey, S. Z. Qiao, *Angew. Chem., Int. Ed.* **2020**, 59, 21728; b) D. T. Nguyen, S. W. Song, *J. Power Sources* **2017**, 368, 11.
- [22] a) Y. Cao, Y. Zhu, C. Du, X. Yang, T. Xia, X. Ma, C. Cao, *ACS Nano* **2022**, 16, 1578; b) X. Yu, G. Zhao, C. Liu, C. Wu, H. Huang, J. He, N. Zhang, *Adv. Funct. Mater.* **2021**, 31, 2103214; c) M. Mao, Y. Tong, Q. Zhang, Y. S. Hu, H. Li, X. Huang, L. Chen, L. Gu, L. Suo, *Nano Lett.* **2020**, 20, 6852; d) Y. Wang, Z. Liu, C. Wang, X. Yi, R. Chen, L. Ma, Y. Hu, G. Zhu, T. Chen, Z. Tie, J. Ma, J. Liu, Z. Jin, *Adv. Mater.* **2018**, 30, 1802563.
- [23] S. Dey, J. Lee, S. Britto, J. M. Stratford, E. N. Keyzer, M. T. Dunstan, G. Cibin, S. J. Cassidy, M. Elgamal, C. P. Grey, *J. Am. Chem. Soc.* **2020**, 142, 19588.
- [24] X. Xu, C. Ye, D. Chao, B. Chen, H. Li, C. Tang, X. Zhong, S. Z. Qiao, *Adv. Mater.* **2022**, 34, 2108688.
- [25] Y. Shen, Y. Wang, Y. Miao, M. Yang, X. Zhao, X. Shen, *Adv. Mater.* **2020**, 32, 1905524.
- [26] a) Y. Zhang, J. Xie, Y. Han, C. Li, *Adv. Funct. Mater.* **2015**, 25, 7300; b) M. Walter, K. V. Kravchuk, M. Ibáñez, M. V. Kovalenko, *Chem. Mater.* **2015**, 27, 7452.

- [27] Y. Shen, Q. Zhang, Y. Wang, L. Gu, X. Zhao, X. Shen, *Adv. Mater.* **2021**, *33*, 2103881.
- [28] N. Pour, Y. Gofer, D. T. Major, D. Aurbach, *J. Am. Chem. Soc.* **2011**, *133*, 6270.
- [29] F. F. Wang, Y. S. Guo, J. Yang, Y. Nuli, S. Hirano, *Chem. Commun.* **2012**, *48*, 10763.
- [30] a) J. Zhang, Y. Yan, B. Mei, R. Qi, T. He, Z. Wang, W. Fang, S. Zaman, Y. Su, S. Ding, B. Y. Xia, *Energy Environ. Sci.* **2021**, *14*, 365; b) Q. Han, C. Wu, H. Jiao, R. Xu, Y. Wang, J. Xie, Q. Guo, J. Tang, *Adv. Mater.* **2021**, *33*, 2008180; c) Y. Liu, S. Ma, L. Liu, J. Koch, M. Rosebrock, T. Li, F. Bettels, T. He, H. Pfnür, N. C. Bigall, A. Feldhoff, F. Ding, L. Zhang, *Adv. Funct. Mater.* **2020**, *30*, 2002462.
- [31] J. Rodríguez-Carvajal, *Phys. B* **1993**, *192*, 55.
- [32] Y. Zhu, X. Fan, L. Suo, C. Luo, T. Gao, C. Wang, *ACS Nano* **2016**, *10*, 1529.
- [33] H. Xu, W. Zhu, F. Sun, H. Qi, J. Zou, R. Laine, W. Ding, *Adv. Mater. Technol.* **2021**, *6*, 2000882.
- [34] H. Chen, H. Xu, B. Li, Z. Li, K. Zhang, J. Zou, Z. Hu, R. M. Laine, *App. Surf. Sci.* **2022**, *598*, 153768.
- [35] B. Ravel, M. Newville, *J. Synchrotron Radiat.* **2005**, *12*, 537.
- [36] M. Muñoz, P. Argoul, F. Farges, *Am. Mineral.* **2003**, *88*, 694.
- [37] a) E. G. Nelson, J. W. Kampf, B. M. Bartlett, *Chem. Commun.* **2014**, *50*, 5193; b) C. Liao, B. Guo, D. Jiang, R. Custelcean, S. M. Mahurin, X. Sun, S. Dai, *J. Mater. Chem. A* **2014**, *2*, 581; c) B. Pan, J. Zhang, J. Huang, J. T. Vaughey, L. Zhang, S. D. Han, A. K. Burrell, Z. Zhang, C. Liao, *Chem. Commun.* **2015**, *51*, 6214; d) B. Pan, J. Huang, N. Sa, S. M. Brombosz, J. T. Vaughey, L. Zhang, A. K. Burrell, Z. Zhang, C. Liao, *J. Electrochem. Soc.* **2016**, *163*, A1672; e) O. Mizrahi, N. Amir, E. Pollak, O. Chusid, V. Marks, H. Gottlieb, L. Larush, E. Zinigrad, D. Aurbach, *J. Electrochem. Soc.* **2008**, *155*, A103.
- [38] D. T. Nguyen, R. Horia, A. Y. S. Eng, S. W. Song, Z. W. Seh, *Mater. Horiz.* **2021**, *8*, 830.
- [39] a) B. Liu, T. Luo, G. Mu, X. Wang, D. Chen, G. Shen, *ACS Nano* **2013**, *7*, 8051; b) D. He, D. Wu, J. Gao, X. Wu, X. Zeng, W. Ding, *J. Power Sources* **2015**, *294*, 643; c) L. Zhou, F. Xiong, S. Tan, Q. An, Z. Wang, W. Yang, Z. Tao, Y. Yao, J. Chen, L. Mai, *Nano Energy* **2018**, *54*, 360; d) Z. Chen, Z. Zhang, A. Du, Y. Zhang, M. Men, G. Li, G. Cui, *Chem. Commun.* **2019**, *55*, 4431; e) M. Mao, Z. Lin, Y. Tong, J. Yue, C. Zhao, J. Lu, Q. Zhang, L. Gu, L. Suo, Y. S. Hu, H. Li, X. Huang, L. Chen, *ACS Nano* **2020**, *14*, 1102; f) D. Chen, J. Shen, X. Li, S. Cao, T. Li, W. Luo, F. Xu, *J. Energy Chem.* **2020**, *48*, 226; g) X. Lin, J. Liu, H. Zhang, Y. Zhong, M. Zhu, T. Zhou, X. Qiao, H. Zhang, T. Han, J. Li, *Adv. Sci.* **2021**, *8*, 2002298; h) Y. Zhang, Y. Zhu, Z. Wang, H. Peng, X. Yang, Y. Cao, C. Du, X. Ma, C. Cao, *Adv. Funct. Mater.* **2021**, *31*, 2104730.
- [40] H. Liu, H. Guo, B. Liu, M. Liang, Z. Lv, K. R. Adair, X. Sun, *Adv. Funct. Mater.* **2018**, *28*, 1707480.